

# Surface roughness evaluation of additive manufactured metallic components from white light images captured using a flexible fiberscope

Haridas, Aswin; Matham, Vadakke Murukeshan; Crivoi, Alexandru; Patinharekandy,  
Prabhathan; Jen, Tan Ming; Chan, Kelvin

2018

Haridas, A., Matham, V. M., Crivoi, A., Patinharekandy, P., Jen, T. M., & Chan, K. (2018).  
Surface roughness evaluation of additive manufactured metallic components from white  
light images captured using a flexible fiberscope. *Optics and Lasers in Engineering*, 110,  
262-271. doi:10.1016/j.optlaseng.2018.05.026

<https://hdl.handle.net/10356/141762>

<https://doi.org/10.1016/j.optlaseng.2018.05.026>

---

© 2018 Elsevier Ltd. All rights reserved. This paper was published in *Optics and Lasers in Engineering* and is made available with permission of Elsevier Ltd.

*Downloaded on 13 Mar 2024 19:04:05 SGT*

# Surface Roughness Evaluation of Additive Manufactured Metallic Components from White Light Images Captured using a Flexible Fiberscope

Aswin Haridas<sup>b</sup>, V.M. Murukeshan<sup>a,\*</sup>, Alexandru Crivoi<sup>b</sup>, P. Prabhathan<sup>b</sup>, Tan Ming Jen<sup>a</sup> and Kelvin Chan<sup>c</sup>

<sup>a</sup> School of Mechanical and Aerospace Engineering, 50 Nanyang Drive, Nanyang Technological University, Singapore 639798

<sup>b</sup> Rolls-Royce @ NTU Corporate Laboratory, 65 Nanyang Drive, Nanyang Technological University, Singapore 637460

<sup>c</sup> Rolls-Royce Singapore, 6 Seletar Aerospace Rise, Singapore 797575

## ARTICLE INFO

### Keywords:

Surface Roughness  
White light imaging  
Additive Manufacturing  
Image Processing  
Applied Optics

## ABSTRACT

The added capabilities of Additive Manufacturing (AM) while processing metallic components have revolutionized the design and manufacturing flexibility of multitudes of aerospace components. However, AM being a stochastic process results in a degraded control of the surface topography of the printed structure and thus requires adequate finishing processes before implementation. Particularly, in the case of components having complex cross-sections and internal channels, none of the currently available technologies offer a solution for the measurement and certification of surface roughness parameters. In this context, this paper investigates a binary image processing technique applied to multiple white light images captured by a 0.3 mm diameter micro fiber endoscope. Further, AM sample surfaces generated by different build angles are investigated to demonstrate the advantages of the proposed technique. A surface roughness evaluation parameter is presented along with measurement results obtained using the Mitutoyo SJ400 (conventional profiler) and the Talyscan 150 (optical profiler).

## 1. Introduction

The role of AM has tremendously increased the overall process efficiency of large-scale manufacturing owing to its flexibility towards part design and a structured approach that translates onto a highly cost-effective manufacturing technique [1, 2]. Contrary to conventional manufacturing systems, AM offers a higher degree of freedom which allows for the production of a new generation of complex and efficient internal channels for multiple applications such as internal coolant systems [3].

These rising requirements in the design and manufacturing of working components have imposed stringent requirements on the metrology forefront. Essentially, it can be predicted that the futuristic measurement systems must go hand in hand with the manufacturing process, thereby improving their standards in real-time [2]. One such parameter that is of great concern in determining the credibility of the manufacturing process is the surface quality of the manufactured component [4, 5]. Surface measurements play an important role in achieving the desired quality for a metallic component thereby determining its average life-cycle [5]. As per the ISO 25178 part 6 (2010), conventional surface topography evaluation techniques can be broadly categorised into line techniques, areal techniques and area integrating techniques [6]. The line profiling instruments such as contact based stylus and line-scanning mode phase shifting interferometer produces a 2D plot of the surface height distribution [7, 8].

Further, the measurement data can be mathematically represented as a height function  $h(y)$ . Areal topography methods, on the other hand, produce a 3D topographical image of the surface which can then be mathematically represented as  $h(x, y)$ . Techniques such as White Light Interferometry (WLI) [9], Confocal microscopy [10, 11] and focus variation [12] are grouped under this category. In contrast, the areal-integrating methods, such as optical scattering [13] and speckle based techniques including, contrast [14-16], correlation [17-22] and image [23, 24] analysis only provide a statistical representation of the surface under study.

These traditional surface topography evaluation techniques serve well in bench top applications for various AM components. However, one of the most significant point to be considered in the context of the design and development of advanced manufacturing techniques is the suitability of the mentioned techniques for evaluating the surface topography of areas hard-to-access and internal channels. Current available techniques for internal channel inspections either require the sample to be cut [25], necessitates expensive hardware [26] or utilize non-flexible probes [27]. Hence to address these issues, a flexible, easily maneuverable, miniature probe based surface topography evaluation system is envisaged.

In this context, this paper proposes and illustrates a new binary image analysis technique to quantify the surface roughness variations on AM components based on images captured using a 0.3 mm diameter flexible borescope. The use of optical fibers for imaging hard-to-access areas have been studied by various researchers [28-31]. Surface images captured from three AM samples generated using different build angles are compared for validating the process algorithm. Furthermore, the outcome of the technique is validated using conventional and optical stylus measurement systems, namely, Mitutoyo SJ-400 and Talyscan 150.

\* Corresponding author. Tel./fax: (+65) 6790 4200.  
E-mail address: mmurukeshan@ntu.edu.sg (V.M. Murukeshan)

## 2. Materials and Method

This section details the AM samples used for the trials along with the optical test arrangements adopted for this investigation.

### 2.1. AM Sample Details

The AM samples used for the tests are manufactured using the Laser Beam Powder Bed Fusion technique, namely, Direct Metal Laser Sintering (DMLS). The materials used for process is Maraging steel (EOS MS 1) printed with a layer thickness of 40  $\mu\text{m}$ . Figure 1, shows the three samples that are built at 5°, 55° and 75°.

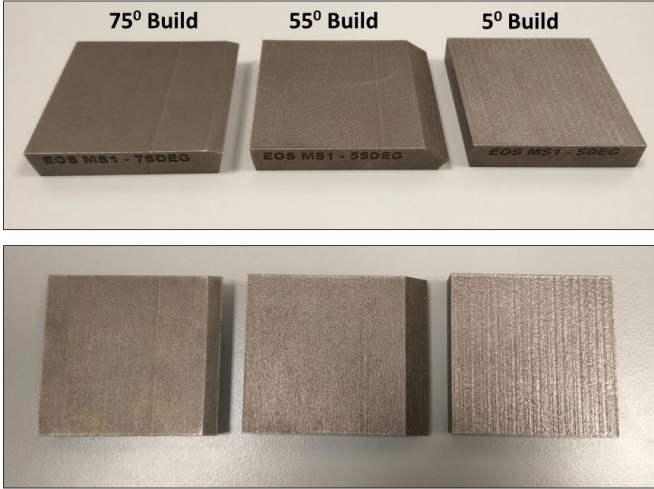


Fig. 1. AM Samples used for the tests with build angles of 5°, 55° and 75° shown to have distinct differences in surface quality.

### 2.2. Experimental Arrangement

The schematic diagram of the experimental setup used for the study of AM samples is presented in Fig. 2. A white light source (Thorlabs-OSL2-High-Intensity Fiber-Coupled Illuminator) coupled with a 0.37 mm diameter optical fiberscope (Myriad Fiber Imaging) illuminates the surface of the sample under study. A spherical imaging lens collects the image of the surface under study and passes it through the imaging fiber (FUJIKURA, FIGH-016-160S) within the fiberscope that contain 1,600 picture elements with a center-to-center pixel spacing of 3.3  $\mu\text{m}$ .

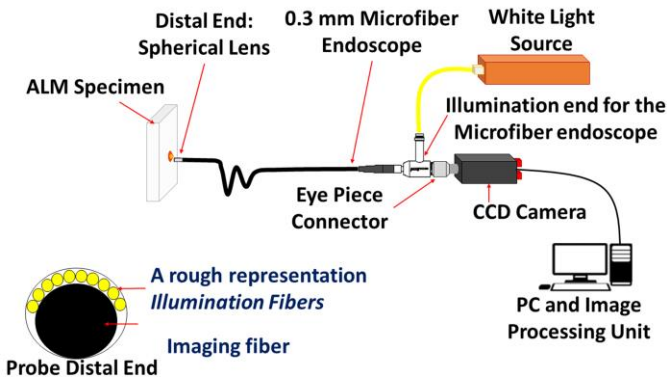


Fig. 2. Experimental arrangement of the optical fiber probe based surface roughness evaluation system.

The eyepiece of the fiberscope is further coupled with a sCMOS camera (ANDOR, XYLA-5.5-sCMOS) using a camera adaptor (Fujikura 30 mm- 60 mm). Figures 3 (a) and 3 (b) show the distal end and the imaging end of the fiberscope, respectively.

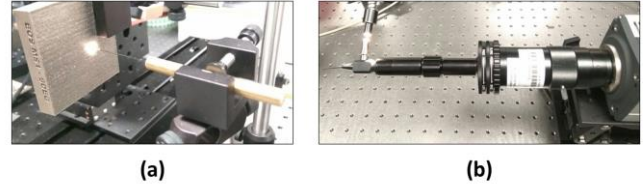


Fig. 3. (a) The distal end illuminating the AM sample and (b) the imaging end coupled with the sCMOS camera using the Fujikura camera adaptor.

### 2.3. Comb Structure Removal/ Fiber De-pixelation Algorithm

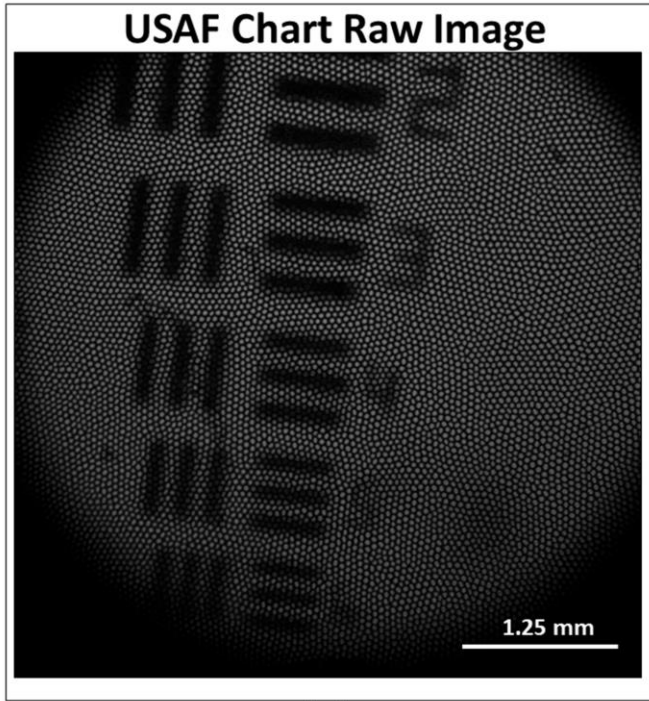
The use of a flexible optical fiberscope leads to the inevitable presence of comb structures that require additional processing for effective pattern recognition and quantitative image analysis [32-34]. In this context, we have investigated multiple static comb structure removal techniques prior to binary image analysis for surface roughness extraction. Three static techniques, namely, frequency filtering, Gaussian filtering and interpolation filtering are investigated to determine the most suitable algorithm for surface roughness extraction using binary image analysis [34].

Spatial averaging technique employs averaging filters to increase the intensity values at darker pixels with respect to the brighter pixels, thereby, reducing the comb structures. An averaging kernel, a spatial filter matrix, is traversed over individual pixels modifying and smoothing the overall image. Gaussian filtering utilizes a kernel that represents a Gaussian filter to remove the comb structures [35]. One drawback in employing spatial averaging techniques for comb removal arises from the choice of kernel itself. The use of spatial averaging filters results in the loss of high frequency information from the image due to its inability to localize the frequencies of the comb structure itself.

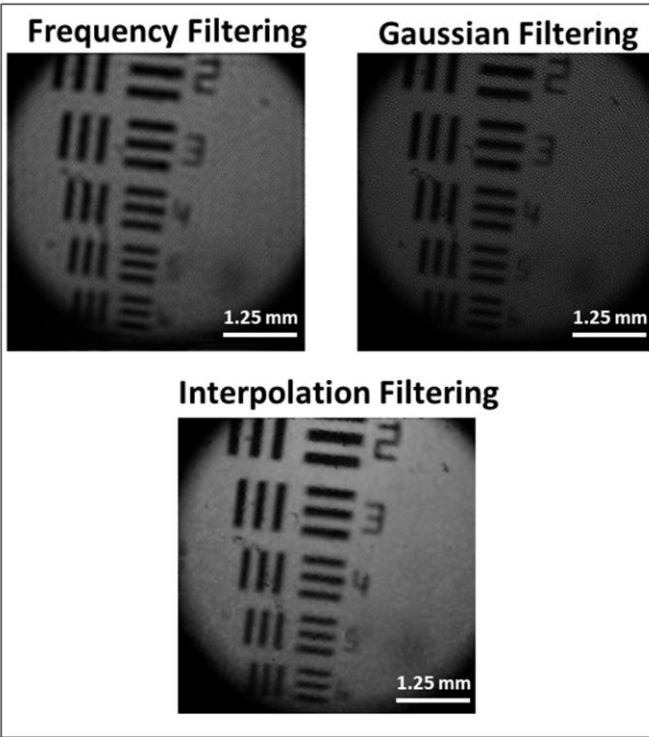
Frequency filtering technique removes high frequency components corresponding to comb structures in the image captured by the fiberscope [36]. A two-dimensional Fourier transform converts the captured image from the spatial domain to the frequency domain. Further, filter masks are employed to remove the high frequency components from the transformed image which is then converted back to the spatial domain using a two-dimensional inverse Fourier transform [35]. Compared to Gaussian filtering, the image quality is higher but with the expense of having a higher processing time and lower possibilities of automation [34].

Interpolation technique for comb structure removal utilizes a two-part algorithm designed to exploit the intensity variations between two neighbouring fibers [37]. The first part of the interpolation algorithm localizes the fiber centres based on a calibration image captured by illuminating the distal end using a white light illumination. The second part interpolates the intensity values between two adjacent fibers to form a uniform image [37]. Compared to the other two techniques, the interpolation method requires time-to-time recalibrations. Additionally, the overall processing time is much higher than the two techniques, a disadvantage in the context of an in-process measurement.

Figure 4 (a), shows an example of a resolution chart (1951 USAF resolution test chart) imaged using a flexible fiberscope (100K fibers with GRIN lens at the distal end) processed using the three-different comb structure (or de-pixelation) techniques (Fig. 4 (b)). Compared to the processing time required for Gaussian filtering, frequency and interpolation filtering multiplied the processing time by a factor of 3 and 10, respectively.



(a)



(b)

Fig. 4. (a) Illustrates the raw image of the USAF chart captured by a flexible fiberscope (FUJIKURA, FIGH -100-1500N; Grin Lens). (b) Processed images using different static comb removal techniques.

#### 2.4. Image Collection

Multiple trials are conducted to capture the representative images from the AM surfaces. Figure 5 describes the methodology implemented for data capture keeping in mind the required statistical significance. For the first sample (In Fig. 5, AM sample with a  $5^\circ$  build angle is shown as an example), a total of 5 images are captured at each of the 10 locations, starting from the center and separated by 0.5 mm each perpendicular

to the visible lay angle (Controlled by a THORLABS LTS long travelling stage).

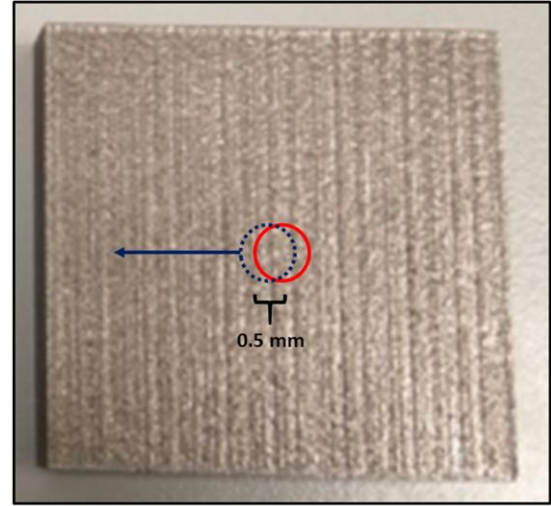


Fig. 5. Represents the methodology implemented for data capture. 5 images captured at each location (indicated by the red circle) for 10 different locations each shifted by 0.5 mm (Indicated by the dotted blue circle).

Figure 6 depicts the flowchart used for image capture and processing and Fig. 7, illustrates the white light images captured at the same location for the AM samples with a  $5^\circ$ ,  $55^\circ$  and  $75^\circ$  build angles, respectively. Further, Fig. 7 also shows the processed images after the three-different static comb structure removal techniques are applied.

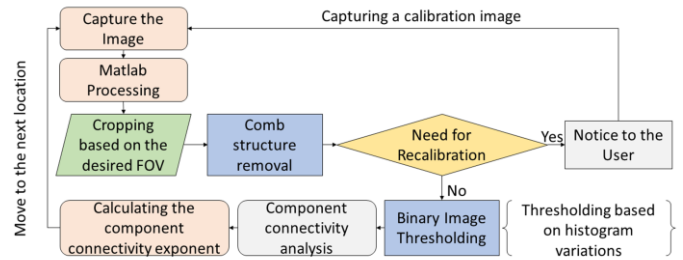


Fig. 6. The flowchart of the proposed methodology.

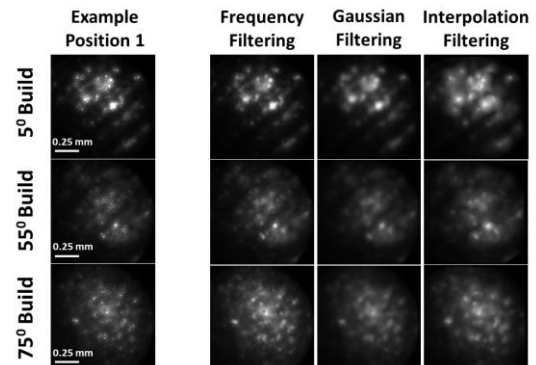


Fig. 7. White light images observed for the three samples through the optical fiberscope along with the processed images using frequency, Gaussian and interpolation filtering.



## 2.4. Binary Image Analysis for Surface Roughness Inspection

De-pixelation and normalization of the images are carried out and the images are binarized using fixed thresholds. Five thresholds values are chosen covering the entire range within the image histogram such that, even the subtle intensity variations can be observed within the binary image, as shown in Fig. 8. Further, the component connectivity parameter from each of the binary image is determined using the algorithm proposed in our previous work [24].

In the context of binary image analysis, the proposed algorithm determines the component connectivity within each of the binary images to produce a pseudo color representation of the clusters. The cluster covering the maximum number of pixels are always represented in black while the color of the other smaller components is randomly chosen. Additionally, a numerical output from the algorithm plots the variations in the size of the maximum connected component with respect to the chosen thresholds.

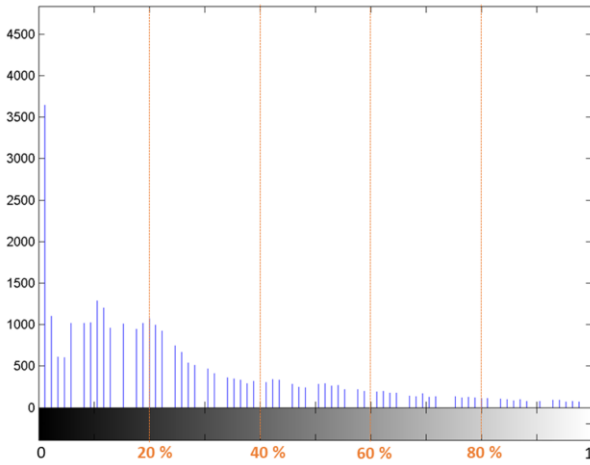


Fig. 8. The chosen thresholds based on the image histogram

## 3. Experimental Results and Discussions

### 3.1. Calculating Component Connectivity Exponent (CCE)

Implementing the binary image threshold followed by the component connectivity analysis algorithm, a pseudo color plot representing the various components together with the component having the largest size (in pixels) can be obtained. In this context, Fig. 9 (a), (b) and (c), illustrates the output of the component connectivity algorithm for frequency filtered, Gaussian filtered and the interpolation filtered image of the AM samples, respectively. While the color black represents the pixels that are part of the component with the largest connections, the pixels containing the smaller components are illustrated using random colors.

Firstly, the dependence of the size and texture of the connected components with the surface topography is evaluated. From Fig. 9 (a), (b) and (c), it is observed that the sample with the 5° build angle show prominent lays at higher thresholds, while the samples build at 55° and 75° do not show any characteristic pattern within the specified threshold values. This remains consistent with the visually observed surface structure of the three samples shown in Fig. 1. Thus, in general, it can be stated that a highly scattering surface results in components that are small and dispersed, while the connected components of a surface with characteristic lays reflect on the lay structure itself.

Secondly, from Fig. 9 (a), (b) and (c), the dependence of the de-pixelation algorithm on the calculated component connectivity is assessed. It can be observed that the frequency filtering technique for comb structure removal results in producing high frequency information

from the captured image. This is evident from the size of the smallest component and the edge definitions of the largest component. However, in the case of Gaussian and Interpolation filtering, the size of the connected component is observed to be wrongly estimated within the chosen threshold range.

The loss of high frequency information for Gaussian filtering algorithm arise from the limitations in optimizing the size and shape of the averaging kernel. Errors in size and shape of the chosen Kernel may result in the loss of high frequency information captured from the sample surface. In the case of Interpolation filtering, errors in spatial calibration of individual fiberlets could lead to the suppression of high frequency information content. However, for frequency filtering, the ease of removing high frequency comb structures from the two-dimensional Fourier transform results in lower errors in choosing the correct frequency filters.

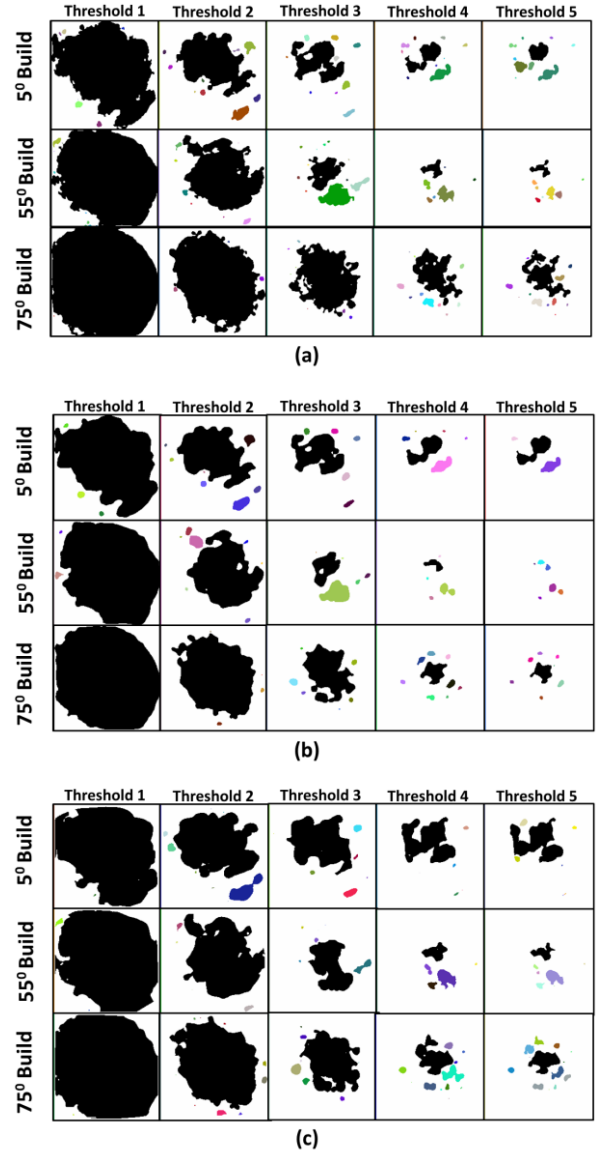


Fig. 9. Component connectivity of the (a) frequency, (b) Gaussian and (c) Interpolation filtered images of the AM samples.

In order to further enhance the investigation, the size of the largest connected component (in pixels) is calculated. Figure. 10 (a), (b) and (c), compares the size of the largest connected component in relation with three variables, namely, applied threshold, de-pixelation technique used and the AM sample build angle. A confidence interval of 95 % is used for this study.

From Fig. 10 (a), (b) and (c) it is observed that for threshold 1, the largest connected component of the AM sample having a 5° build angle (visually having a stronger lay structure in comparison to the AM samples having 55° and 75° build angles) covers the smallest number of pixels. In comparison, the largest connected component of the samples having 55° and 75° build angles is observed to cover more pixels. This behaviour could be attributed to lack of visible lays on these samples. Therefore, compared to the sample having a 5° build angle a broader component connectivity due to a higher degree of scatter is observed.

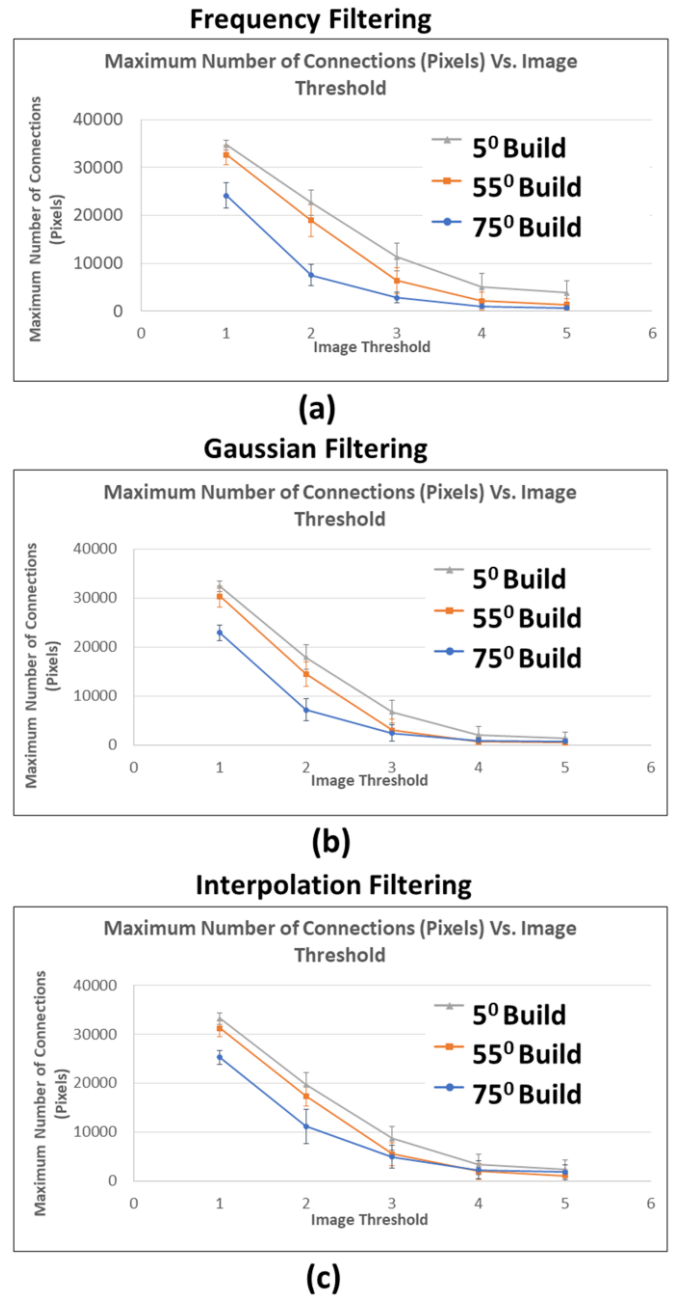


Fig. 10. Quantitative comparison of connected components with respect to the chosen thresholds, comb structure removal technique and the AM sample build angle (Confidence Interval: 95%). (a) Frequency Filtered, (b) Gaussian Filtered and (c) Interpolation Filtered.

Additionally, by studying the exponential behaviour of component connectivity for threshold 1 through 5, assessment of surface similarities can be made. For example, in figure. 10 (a), the largest connected component for the sample having the 55° build angle at threshold 1

covers 20% more pixels than the sample having the 5° build angle but 5% lesser pixels than the sample having the 75° build angle. However, for higher thresholds, this trend reverses. This could be attributed to the sample with the 55° build angle having surface topography features that can be linked to the other two samples.

Therefore, in order to improve the quantitative analysis incorporating the information content with increasing values of threshold, a new surface topography parameter is introduced. The new parameter termed, Component Connectivity Exponent (CCE), represents the exponential variation of the largest connected component with increasing values of threshold. The CCE is calculated as the modulus of the exponent parameter  $B$  (in  $Ae^{-Bx}$ ) from the general equation of a negative exponential curve. Where,  $A$  represents a constant and variable  $x$  is the chosen thresholds. Table 1, depicts the calculated CCE for each of the samples whose images are evaluated using the three-different comb structure removal techniques.

Table 1

Component Connectivity Exponent (CCE) comparison for the AM samples considered. The CCE is calculated separately for each of the comb filtering technique applied.

Sample Build angle	Component Connectivity Exponent (CCE)		
	Frequency Filtering	Gaussian Filtering	Interpolation Filtering
5°	0.91	0.68	0.68
55°	0.85	1	0.89
75°	0.59	0.85	0.70

### 3.2. Measurement Validation using Mitutoyo SJ400 and Talyscan 150

In order to demonstrate the capability of CCE for surface topography evaluation, validation studies were carried out using the conventional and optical stylus profilometers Mitutoyo SJ400 and Talyscan 150, respectively.

2D Surface roughness parameters was measured using the Mitutoyo SJ400 to determine the compatibility of the proposed technique with the current industrial standards. In these tests, 9 lines were drawn with 5 replicates at each location to ensure repeatability and statistical significance. The average surface roughness measured from the 2D surface height profile  $h(y)$  is tabulated in Table 2. Figure 11 (a), (b) and (c) show the variation of CCE with the  $R_a$  measured using the stylus profilometer. Further, the study is extended to compare the influence of two additional parameters, namely, the comb removal technique used and the AM sample build angle.

Table 2

Average surface roughness ( $R_a$ ) measured using the conventional stylus Mitutoyo SJ400

Sample Build angle	Stylus Measurement
	$R_a$ ( $\mu\text{m}$ )
5°	$11.82 \pm 0.78$
55°	$10.72 \pm 1.14$
75°	$4.15 \pm 0.36$

From Fig. 11, it can be observed that the exponential parameter (CCE) varies proportional to the  $R_a$  measured using the conventional stylus with a good statistical significance (95% Confidence Interval (CI)). However, from Fig. 11 (a), (b) and (c), it can be observed that the CCE calculated and the  $R_a$  measured are in good agreement for the images processed using the frequency filtering technique. For the sample with the 5° build angle, the CCE values calculated for the images processed using Gaussian and the Interpolation filter are observed to be underestimated. This could be attributed to an overestimated pixel

coverage of the largest connected component due to the presence of low frequency surface lays. Similarly, higher values of CCE observed for 55° and 75° build angles could be due to an underestimated pixel coverage of the largest connected component in the absence of low frequency surface features.

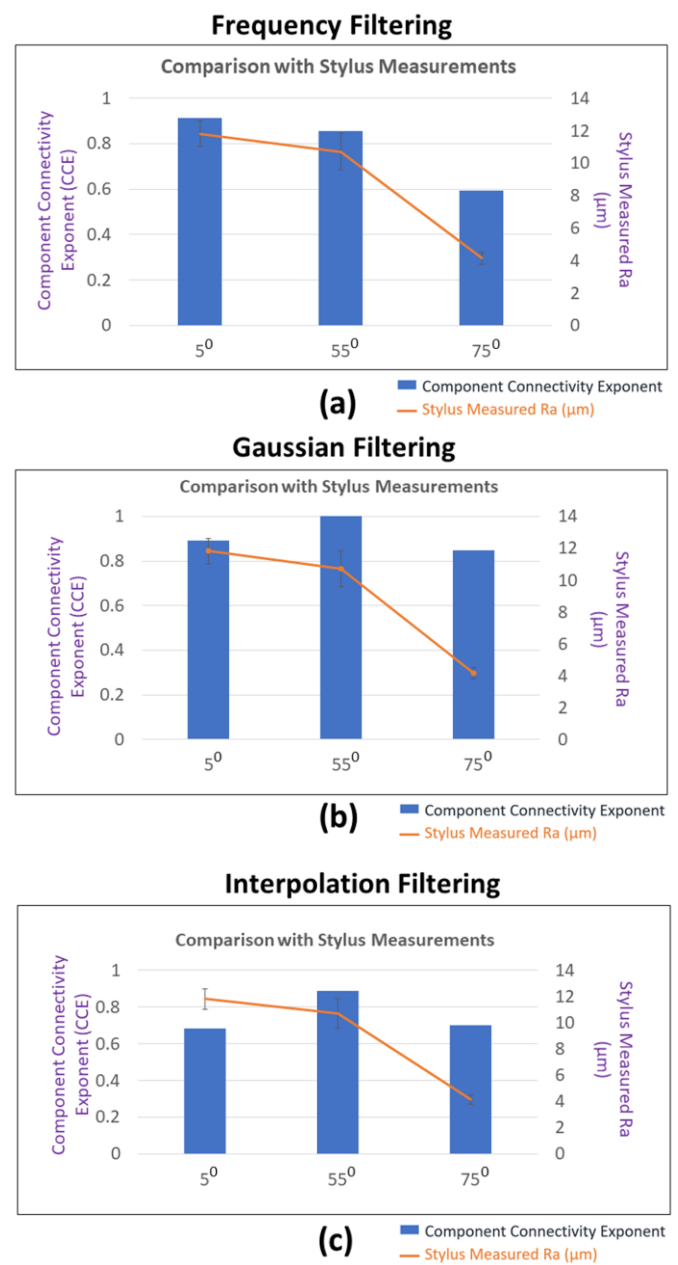


Fig. 11. Component Connectivity Exponent (CCE) in comparison with stylus profilometer (Mitutoyo SJ400) for surface roughness evaluation of the ALM samples with (a) 5°, (b) 55°and (c) 75° build angles, respectively

In order to validate the capability of CCE in topography estimation, 3D surface topography was generated using the Talyscan 150 optical stylus profiler. An area of 5 mm x 2 mm is chosen (ISO 25178 part 6 (2010)) with a scanning resolution of 5 μm. Figure 12 (a), (b) and (c), shows the surface topography measured for each of the AM samples using the Talyscan 150 optical profiler.

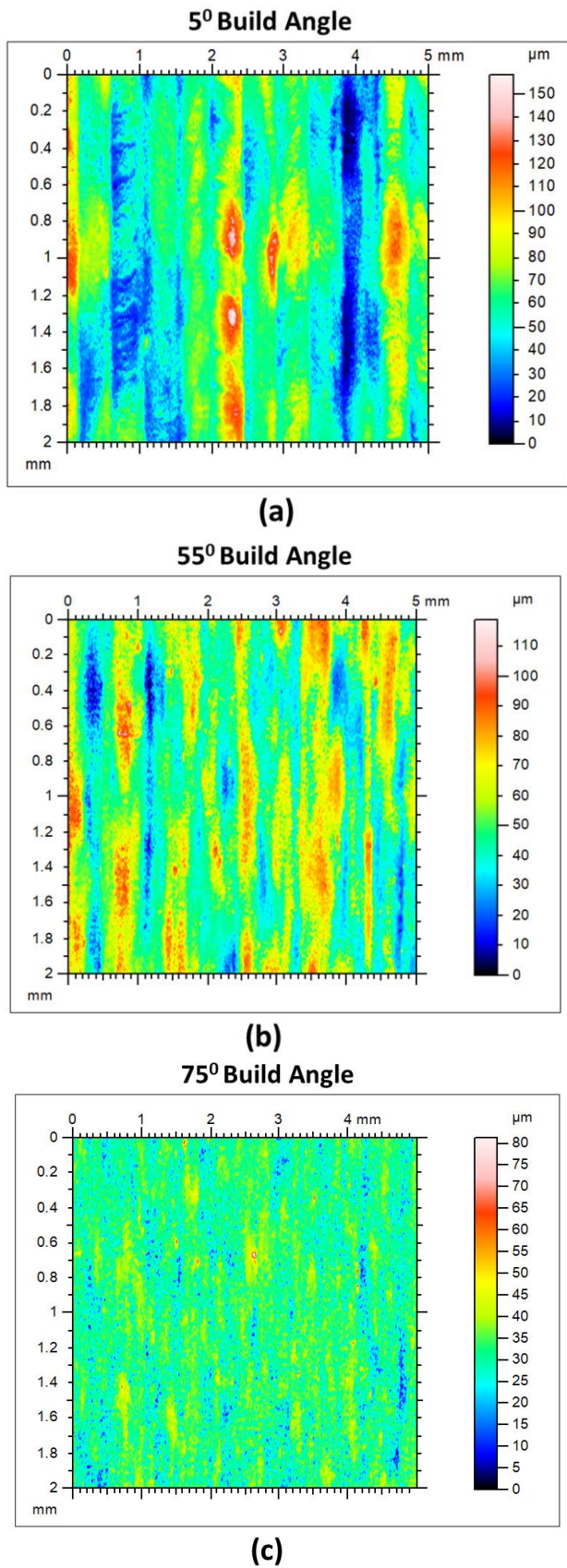


Fig. 12. The measured surface topographies for samples with (a) 5°, (b) 55°and (c) 75° build angles, respectively

Table 3  
Surface roughness parameters measured using the Taylor Hobson Talyscan 150

Sample Build angles	Talyscan 150					
	Sa (μm)	Sq (μm)	Ssk	Sku	Sp (μm)	Sv (μm)
5°	9.25 ± 0.05	11.7 ± 0.05	0.66 ± 0.03	3.80 ± 0.53	60.30 ± 1.31	44.08 ± 0.70
55°	8.40 ± 0.15	10.3 ± 0.01	0.33 ± 0.04	2.88 ± 0.05	46.60 ± 0.48	36.60 ± 0.28
75°	3.87 ± 0.15	4.82 ± 0.04	-0.26 ± 0.02	4.75 ± 0.85	37.50 ± 1.76	20.92 ± 0.47

In order to quantitatively characterize the areal surface topography of the samples multiple roughness parameters are extracted and tabulated in Table 3.

Figures. 13 (a), (b) and (c) show the variation of CCE with the areal surface roughness parameters Sa and Sq, measured using the Talyscan 150. From Fig. 13, it can be observed that the exponential parameter (CCE) varies in sync with both Sa and Sq with a good statistical significance (95% Confidence Interval (CI)). From Fig. 13 (a), (b) and (c), it can be observed that the CCE calculated and Sa and Sq measured are in good agreement for the images processed using the frequency filtering technique. This is analogous to the observation made in section 3.2 while comparing the 2D surface roughness parameter with CCE.

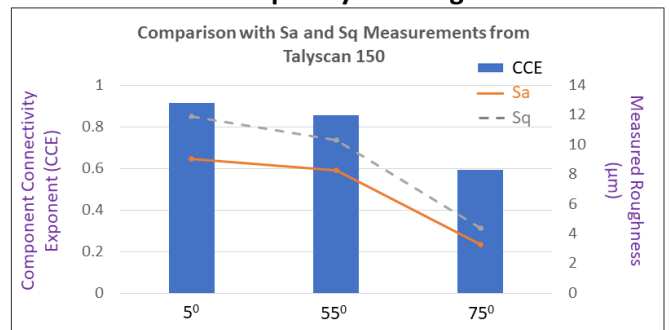
However, in order to determine the effectiveness of the proposed technique in surface classification based on surface topography, the skewness parameter, Ssk, and the Kurtosis parameter, Sku are calculated.

In theory, for a Gaussian (random) surface the Ssk parameters tends to zero. However, for samples with surfaces having bulk of its profile peaks above or below the mean plane, the skewness (Ssk) value would either be negative or positive, respectively. From Table 3, the samples having 5° and 55° build angles are observed to have positive skew values, while the sample having a 75° build angle is observed to have a negative skew value. This suggests that bulk of the surface profile of the former is below the mean plane, while bulk of the surface profile of the latter is above the mean plane. Additionally, from Table 3, it can be observed that for the sample having a 75° build angle, the Ssk value is the closest to zero. This validates the higher degree of scatter and broader component connectivity's observed in section 3.1.

The kurtosis parameter is a measure of the sharpness the roughness profile. A normal height distribution would have an Sku value equal to three. However, for height distributions that are skewed about the mean plane or spiked, the Sku values would be lesser than or greater than 3, respectively. From table 3, while the sample having a 55° build angle is observed to have an Sku value close to 3, the samples having 5° and 55° build angles have an Sku value greater than 3.

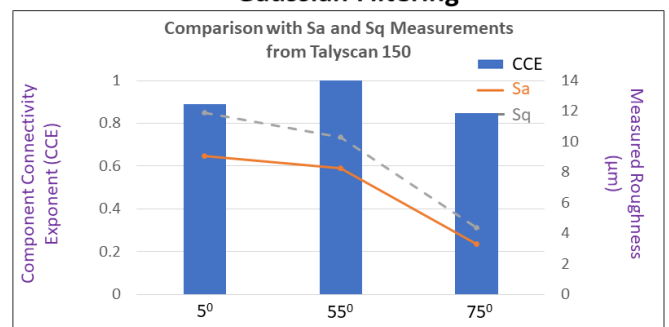
Additionally, in order to determine the measurement sensitivity of the proposed method, amplitude parameters including the Sp and Sv are calculated. Sp is the absolute value of the height of the largest trough and Sv is the absolute value of the height of the largest pit within the defined area. Figures. 14 (a), (b) and (c) show the variation of CCE with the parameters Sv and Sp, measured using the Talyscan 150. The variation of CCE with Sv and Sp for the samples. The sensitivity of CCE in measurement of Sv and Sp can be utilized to eliminate height distributions beyond the desired levels.

### Frequency Filtering



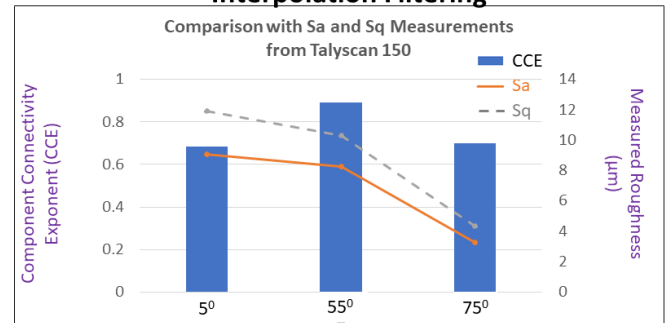
(a)

### Gaussian Filtering



(b)

### Interpolation Filtering



(c)

Fig. 13. Component Connectivity Exponent (CCE) in comparison with the Sa and Sq parameters calculated using an optical profiler (Talyscan 150) for surface roughness evaluation of the ALM samples with (a) 5°, (b) 55° and (c) 75° build angles, respectively



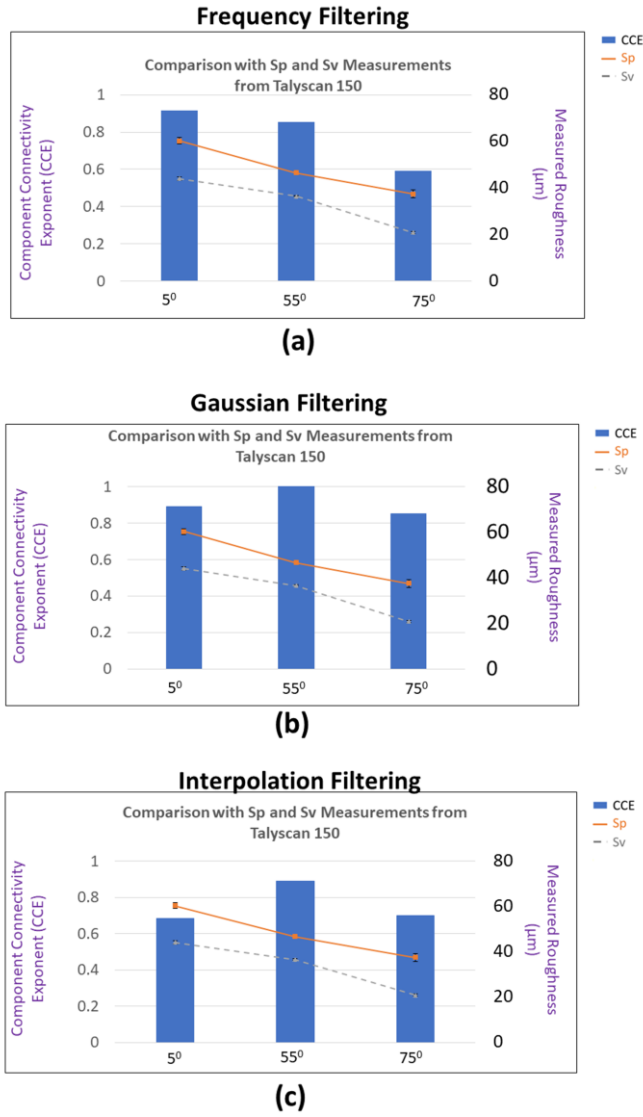


Fig. 14. Component Connectivity Exponent (CCE) in comparison with the Sp and Sv parameters calculated using optical profiler (Talyscan 150) for surface roughness evaluation of the ALM samples with (a) 5°, (b) 55° and (c) 75° build angles, respectively

### 3.3. Measurement time comparison

In order to evaluate the advantages of the proposed method, the time taken for measurements are assessed. The time taken for measurements using the proposed technique and the conventional technique used for validation are given in Table 4. The total time for image collection and binary image processing using the proposed technique (~ 130 seconds) is observed to be much lesser than the conventional Talyscan 150 (~ 860 seconds). An Intel Core i5-5200U processor was used.

Table 4  
Time for measurements: Proposed and validation techniques

			Time (Sec)
			~ 120
Proposed Techniques	Image Collection		
	Image	Frequency	2.55
	Depixelation	Gaussian	0.87
		Interpolation	9.25
		CCE Calculation	2.23
Validation Techniques	Mitutoyo SJ 400 (4 mm)		9 ± 0.5
	Talyscan 150 (5 mm x 2 mm)		860 ± 30

### 3.4. Influence of sample tilt on CCE measurement

One of the applications envisaged for the proposed probe is for measuring areas that are hard-to-access. In this context, the position of the distal end of the probe with respect to the specimen becomes critical. Therefore, parameters such as the illumination and imaging angles are influential factors for CCE measurement. However, as the distal end design for the probe is fixed (shown in Fig. 1), the influence of sample tilt on CCE is studied.

Figure 15, shows the experimental arrangement to study the influence of specimen tilt on CCE measurements. A rotational stage (THORLABS RP01) having a precision of 1° is used for the experiments. A range of angles from -20° to +20° with 2° intervals are chosen. At each position of the rotational stage 10 images are collected.

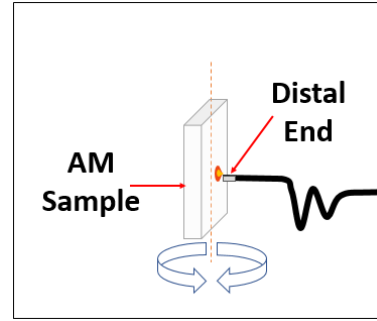


Fig. 15. Sample arrangement to determine the effect of specimen tilt on CCE calculation.

Figure 16 (a) and (b), shows the images of the samples having a 5° build imaged at 0° and +20°, respectively. As the tilt angle increases, scattering and shadowing effects were seen to be dominant. Figure 16 (c), shows the variation of the measured CCE with respect to the sample tilt for each of the Depixelation algorithms chosen. As expected, the CCE values dropped as the specimen tilt was increased. This analogy was found to be consistent with all the depixelation algorithms considered.

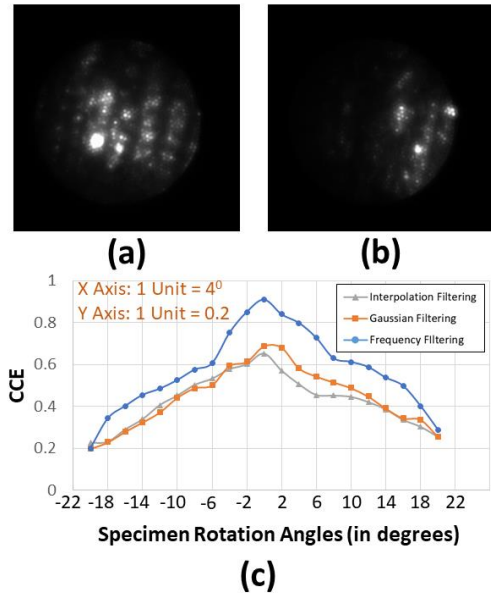


Fig. 16. (a) and (b) shows the images of the samples having a 5° build imaged at 0° and +20°, respectively. The variation of CCE with specimen tilt for different Depixelation algorithms used is shown in (c).

#### 4. Conclusions

Surface roughness measurement of AM components is a critical problem owing to its stochastic nature particularly for components containing internal channels or hard-to-access areas. In order to meet these requirements a new image processing technique is developed to quantitatively characterize areal roughness from images captured using an existing 0.3 mm diameter flexible fiberscope. A set of 10 white light images are captured from the surface of each of the three different AM samples having a 5°, 55° and 75° build angles. Prior to binary image analysis static comb structure removal algorithms, namely, frequency, Gaussian and interpolation filtering are implemented to remove the high frequency fiber pixelation. Further, the images are binarized by employing fixed thresholds determined by the intensity distribution within the image histograms. Component connectivity analysis is performed on these binarized images to determine the variations in component sizes with respect to the applied thresholds. A parameter, Component Connectivity Exponent (CCE) is introduced to differentiate the surface profiles of the three samples based on surface reflectivity. The measurement results are compared with the Mitutoyo SJ-400 and the Talyscan 150. 2D and 3D surface roughness were used to validate the proposed method.

Each of the samples were studied to determine the correlation of CCE with respect to the measured surface roughness parameters. The variation of CCE values for the three different samples were seen to be attributed to two main factors, the de-pixelation algorithm chosen and the surface topography itself. Frequency filtering technique was observed to be effective in obtaining high frequency sample information compared to the Gaussian and the interpolation filtering techniques. In the case of Gaussian and interpolation filtering, the high frequency components of surface scatter were filtered leading to a positive drift in the measured value of CCE, especially for the samples with the 55° and 75° build angles. The proposed technique took lesser time for measurements in comparison to the conventional systems. The CCE parameter was also seen to be strongly dependent on the specimen tilt.

Future work in this research will be to understand the Key Performance Variables (KPV's) of the system and perform statistical tests to determine the most significant parameter for surface roughness inspection. On the instrumentation front, the developed optical probe will be subjected to modified configuration to enable testing of complex internal channels on AM components. An optimization study on developing suitable side view probes to image side walls of the internal channel will also be explored. It is envisaged that the proposed methodology and developed probe system can be applied for real-time inspections of internal channels and hard-to-access areas, thereby improving the AM manufacturing process.

#### Acknowledgments

This work was conducted within the Rolls-Royce@NTU Corporate Lab MRT 4.1 project with support from the National Research Foundation (NRF) Singapore under the Corp Lab@University Scheme. The authors are also grateful for the support from COLE EDB funding. One of the authors P. Prabhathan contributed to this work during his role as a research fellow at Rolls-Royce@NTU Corporate Lab. Also, Aswin Haridas acknowledges the financial support received through NTU under the RSS scheme.

#### References

- [1] Andrew T, Giusca C, Macaulay G, Roerig F, Hoebe M, Leach R, et al. Surface texture measurement for additive manufacturing. *Surface Topography: Metrology and Properties* 2015; 3(2): 024002.
- [2] Uriondo A, Esperon-Miguez M, Perinpanayagam S. The present and future of additive manufacturing in the aerospace sector: A review of important aspects. *Proceedings of the Institution of Mechanical Engineers, Part G: Journal of Aerospace Engineering* 2015; 229(11): 2132-2147.

- [3] Pietropaoli M, Ahlfeld R, Montomoli F, Ciani A, D'Ercole M. Design for Additive Manufacturing: Internal Channel Optimization. *J. Eng. Gas Turbines Power* 2017; 139(10): 102101
- [4] Bons J. A review of surface roughness effects in gas turbines. *Journal of turbomachinery* 2010; 132(2): 021004.
- [5] Field M. Surface integrity—a new requirement for improving reliability of aerospace hardware. in *Proceedings of 18th annual national SAMPE symposium* 1973.
- [6] Leach R. *Optical Measurement of Surface Topography*. Berlin, Heidelberg: Springer-Verlag Berlin Heidelberg; 2011.
- [7] Vorburger T, Rhee H, Renegar T, Song J, Zheng A. Comparison of optical and stylus methods for measurement of surface texture. *The International Journal of Advanced Manufacturing Technology* 2007; 33(1-2): 110-118.
- [8] Schreiber H, Bruning J. Phase Shifting Interferometry, in *Optical Shop Testing*: John Wiley & Sons Inc; 2006, p.547-666.
- [9] Windecker R, H.J. Tiziani. Optical roughness measurements using extended white-light interferometry. *Optical Engineering* 1999; 38(6): 1081-1087.
- [10] Blateyron F. Chromatic Confocal Microscopy, in *Optical Measurement of Surface Topography*, R. Leach, Editor. Springer Berlin Heidelberg: Berlin, Heidelberg; 2011, p.71-106.
- [11] Fuseler J, Jerome W, Price R. Types of Confocal Instruments: Basic Principles and Advantages and Disadvantages, in *Basic Confocal Microscopy*, R.L. Price and W.G. Jerome, Editors. Springer New York: New York, NY; 2011, p.157-179.
- [12] Danzl R, F Helml, Scherer S. Focus variation—a robust technology for high resolution optical 3D surface metrology. *Strojniški vestnik-Journal of mechanical engineering* 2011; 57(3): 245-256.
- [13] Bennett J. Surface roughness and scattering. in *The Proceedings of The Manufacturing & Machine Tool Conference 5 2004*. The Japan Society of Mechanical Engineers.
- [14] Goodman J. Dependence of image speckle contrast on surface roughness. *Optics Communications* 1975. 14(3): 324-327.
- [15] Persson U. Real time measurement of surface roughness on ground surfaces using speckle-contrast technique. *Optics and lasers in engineering* 1992. 17(2): 61-67.
- [16] Prabhathan P, Song C, Haridas A, Prasad G, Chan K. Intensity and contrast based surface roughness measurement approaches for rough and shiny surfaces. *Proc. SPIE, Fifth International Conference on Optical and Photonics Engineering* 2017.
- [17] Dev K, Prasad G, Haridas A, Prabhathan P, Chan K, Murukeshan V. Surface roughness measurement of additive manufactured samples using angular speckle correlation. *Proc. SPIE, Fifth International Conference on Optical and Photonics Engineering* 2017.
- [18] Persson U. Measurement of surface roughness on rough machined surfaces using spectral speckle correlation and image analysis. *Wear* 1993. 160(2): 221-225.
- [19] Persson U. Surface roughness measurement on machined surfaces using angular speckle correlation. *Journal of Materials Processing Technology* 2006. 180(1): 233-238.
- [20] Prabhathan P, Song C, Haridas A, Prasad G, Chan K, Murukeshan V. Experimental investigations and parametric studies of surface roughness measurements using spectrally correlated speckle images. *Proc. SPIE, Fifth International Conference on Optical and Photonics Engineering* 2017.
- [21] Ruffing B. Application of speckle-correlation methods to surface-roughness measurement: a theoretical study. *JOSA A* 1986; 3(8): 1297-1304.
- [22] Spagnolo G, Paoletti D, Paoletti A, Ambrosini D. Roughness measurement by electronic speckle correlation and mechanical profilometry. *Measurement* 1997. 20(4): 243-249.
- [23] Hamed A, Ghandoor H, Diasty F, Saady M. Analysis of speckle images to assess surface roughness. *Optics & Laser Technology* 2004; 36(3): 249-253.
- [24] Haridas A, Crivoi A, Prabhathan P, Chan K, Murukeshan V. Fractal speckle image analysis for surface characterization of aerospace structures. *Proc. SPIE, Fifth International Conference on Optical and Photonics Engineering* 2017.
- [25] Donsheng Y, Zhenqing C, Ke H. Roughness Measurement of Micro-hole Processed by Laser. *Tool Engineering* 2003; 10: 025.
- [26] Kobayashi T, Shan X, Murakoshi Y, Maeda R. A novel self-sensitive SFM for nondestructive measurement of tiny vertical surfaces with restricted access. in *Design, Test, Integration and Packaging of MEMS/MOEMS. Symposium on*. 2003. IEEE.
- [27] Xu X, Liu S, Hu H. A new fiber optic sensor for inner surface roughness measurement. *Proc. SPIE, International Conference on Optical Instruments and Technology: Advanced Sensor Technologies and Applications* 2009.
- [28] Padmanabhan S, Shinoj V, Murukeshan V, Padmanabhan P. Highly sensitive optical detection of specific protein in breast cancer cells using microstructured fiber in extremely low sample volume. *J. Biomed. Opt* 2010; 15(1) 017005.
- [29] Sujatha N, Murukeshan V, Ong L, Seah L. An all fiber optic system modeling for the gastrointestinal endoscopy: design concepts and fluorescent analysis. *Optics Communications*. Volume 219 2003; 6(1). 71-79.
- [30] Shinoj V and Murukeshan V. Hollow-core photonic crystal fiber based multifunctional optical system for trapping, position sensing, and detection of fluorescent particles. *Opt. Lett* 2012; 37, 1607-1609.
- [31] Shinoj V, Murukeshan V, Tor S, Loh N, Lye S. Design, fabrication, and characterization of thermoplastic microlenses for fiber-optic probe imaging. *Appl. Opt* 2014; 53, 1083-1088.
- [32] Rupp S, Elter M, Winter C. Improving the accuracy of feature extraction for flexible endoscope calibration by spatial super resolution. in *Engineering in Medicine and Biology Society. EMBS 2007. 29th Annual International Conference of the IEEE*. 2007.
- [33] Han J, Lee J, Kang J. Pixelation effect removal from fiber bundle probe based optical coherence tomography imaging. *Optics Express* 2010; 18(7): 7427-7439.
- [34] Shinde, A, Murukeshan V. Pixelate Removal in an Image Fiber Probe Endoscope Incorporating Comb Structure Removal Methods. *Journal of Medical Imaging and Health Informatics* 2014; 4(2): 203-211.
- [35] Solomon C, Breckon T. *Fundamentals of Digital Image Processing: A practical approach with examples in Matlab*: John Wiley & Sons; 2011.
- [36] Winter C, Rupp S, Elter M, Münzenmayer C, Gerhäuser H, Wittenberg T. Automatic adaptive enhancement for images obtained with fiberoptic endoscopes. *IEEE transactions on biomedical engineering* 2006; 53(10): 2035-2046.
- [37] Winter, C, Zerfass T, Elter M, Rupp S, Wittenberg T. Physically motivated enhancement of color images for fiber endoscopy. *Medical Image Computing and Computer-Assisted Intervention—MICCAI 2007* 2007: 360-367.